electronics

MDPI

Article

AC Fault Ride-Through Strategy for Offshore Wind Power via Diode Rectifier Unit-Based Transmission System

Jinjiao Lin *, Sudi Xu , Wenxuan Lyu and Wei Li

State Grid Jiangsu Electric Power Co., Ltd., Research Institute, Nanjing 211103, China; xsd19940526@126.com (S.X.)
* Correspondence: linjinjiaoyx@126.com

Abstract

The offshore wind power transmission system based on a diode rectifier unit (DRU) high-voltage direct current (HVDC) faces DRU blocking under sending-end AC faults and DC overvoltage under receiving-end AC faults. To address these two types of AC fault scenarios, corresponding fault ride-through strategies are proposed. For sending-end AC faults, a fault ride-through strategy based on active voltage reduction of the receiving-end converter station is proposed. An active voltage reduction control loop based on DC current deviation is added before the original DC voltage control loop of the receiving-end converter station, so that the DC voltage can be adaptively reduced with the decrease in DC current during sending-end faults. Thus, the conduction condition of the DRU is satisfied, and wind power transmission is maintained. For receiving-end AC faults, a fault ride-through strategy based on source-side active power reduction is proposed. According to the coupling relationship between the DC voltage and the wind turbine outlet voltage, an active power reduction control loop based on the outlet voltage deviation is added before the active power control loop of the wind turbine grid-side converter. During receiving-end faults, each wind turbine actively reduces its active power output, thereby suppressing the DC-side power surplus from the source side. The effectiveness of the proposed strategies was further evaluated through comparative simulations. Taking the 50% voltage-sag cases as examples, the proposed strategy maintains the DC current and transmitted power at approximately 0.84 p.u. and 0.42 p.u., respectively, during the sending-end fault, whereas both decrease to zero under the traditional strategy. During the receiving-end fault, the proposed strategy limits the DC voltage to within 1.05 p.u. and stabilizes the sending-end and receiving-end transmitted powers at approximately 0.49 p.u., while avoiding sustained voltage and current oscillations.

Keywords: offshore wind power; high-voltage direct current transmission; diode rectifier unit; sending-end AC fault; receiving-end AC fault; fault ride-through

Check for updates

Academic Editor: Fabio Corti

Received: 11 August 2026
Revised: 9 September 2026
Accepted: 13 September 2026
Published: 16 September 2026

1. Introduction

As offshore wind power develops toward deep, far-sea sites and larger capacities, the economy, reliability, and lightweight design of offshore wind power transmission systems have attracted wide attention [1–4]. The high-voltage direct current based on modular multilevel converter (MMC-HVDC) transmission system has good controllability, but the large size, heavy weight, and high cost of offshore converter platform limit its application in deep-sea wind power development [5–7]. In contrast, a high-voltage direct transmission system based on a diode rectifier unit (DRU-HVDC) adopts DRU as the offshore converter platform, eliminating the need for a fully controlled offshore converter and its complex control system. Owing to its simple structure, low cost, and high reliability, this approach has become one of the important technical solutions for large-scale offshore wind power transmission [8–10].

In offshore wind power transmission systems via DRU-HVDC, the DRU cannot actively establish the sending-end AC voltage, nor can it independently regulate active and reactive power. Therefore, wind turbines must not only perform power control but also support the voltage and frequency of the sending-end AC system. Existing studies generally adopt grid-forming control strategies so that wind turbines can autonomously establish the offshore AC voltage while providing commutation conditions for the diode rectifier. In [11], a phase-locked-loop-based grid-forming control was proposed. When the wind turbine is connected to the grid, the phase of the AC grid is tracked by the phase-locked loop, so that the synchronous grid connection is realized without switching the control mode. In [12], the strong correlations between active power and sending-end voltage and between reactive power and sending-end frequency in a DRU-HVDC system are proved by sensitivity analysis. On this basis, the power outer-loop controllers of P/V and Q/f are constructed. In [13], a Q/f synchronization control method was proposed, and a first-order inertial controller was added to the Q/f control loop to improve the dynamic response characteristics of the control system.

For sending-end AC faults in DRU-HVDC systems, existing studies mainly focus on wind turbine protection and fault current control. In [14], the DC chopper is used to absorb the redundant power during the sending-end AC fault, so as to reduce the power imbalance between the AC and DC sides of the grid-side converter and maintain the stability of the DC capacitor voltage. In [15], a control method that adaptively regulates the fault current based on the voltage deviation was proposed, so that the wind turbine can quickly provide controlled fault current during the fault period, and cooperate with overcurrent protection to realize fault detection and isolation. In [16], a grid-forming control and an adaptive virtual-impedance low-voltage ride-through strategy for the wind turbine grid-side converter were proposed. The fault current is suppressed by dynamically adjusting the equivalent output impedance of the converter, and the voltage and power recovery performance after fault clearance is improved. The above methods can limit wind turbine overcurrent to a certain extent. However, the AC-side voltage of the DRU still drops during sending-end faults. The receiving-end converter station still operates under constant DC voltage control, so the DC-side voltage of the DRU remains at a relatively high level. As a result, all of these methods still suffer from DRU blocking and interrupted power transmission.

For receiving-end AC faults in DRU-HVDC systems, most of the existing studies have followed the method of installing DC choppers in the MMC-transmission system. The DC chopper is used to consume the surplus power during the fault to suppress the overvoltage of the HVDC transmission line. In [11], an active voltage-boosting control strategy for the receiving-end converter station was proposed. During the AC fault at the receiving-end, by rapidly increasing the DC voltage, the positive voltage difference on both sides of the DRU is reduced, and the active power transmitted by the DRU to the DC system is reduced to alleviate the DC line overvoltage caused by the power imbalance between the sending and receiving ends. In [17], while the DC voltage is raised, the port voltage of the wind turbine grid-side converter is also reduced. This further weakens the active power transmission capability of the DRU. The above methods can improve the receiving-end AC fault ride-through capability of DRU-HVDC systems to a certain extent. However, they rely on raising the DC-side voltage or adding energy-dissipation devices, which increases the voltage stress and hardware cost of the system. Neither of them considers the influence of the wind turbines' active power output on the overvoltage.

In summary, existing research on sending-end and receiving-end AC faults in offshore wind power transmission via DRU-HVDC systems still has the following shortcomings:

(1) For sending-end AC faults, existing studies mostly focus on wind turbine protection. During the fault, the receiving-end converter station still maintains a high DC voltage, resulting in the DRU blocking due to the decrease in DC output capacity, which tends to trip the wind turbines and disconnect them from the grid.

(2) For receiving-end AC faults, existing studies mostly rely on a DC chopper to consume the surplus power, or on reducing the power transmission capability of the DRU. They do not actively regulate the active power output of the wind farm, and it is difficult to suppress the power surplus during the fault at the receiving end from the source.

To address the above shortcomings, this paper studies the transient mechanisms and fault ride-through control of DRU-HVDC systems under sending-end and receiving-end AC faults. The main contents are as follows:

(1) For sending-end AC faults, the mechanism of DRU blocking under the traditional wind-turbine current-limiting strategy is analyzed. The active power characteristics of the DC system during the fault are clarified. A fault ride-through control strategy based on active voltage reduction of the receiving-end converter station is proposed. During the fault, the DC voltage of the receiving-end converter station is reduced to maintain the DRU conduction, which can reduce the risk of system shutdown and grid disconnection.

(2) For receiving-end AC faults, the transient mechanism of DC system overvoltage during the fault is analyzed. The coupling relationship between the system DC voltage and the wind turbine outlet voltage is derived. A fault ride-through control strategy based on source-side active power reduction is proposed. During the fault, the active power injected by the wind farm into the DC system is reduced, alleviating the DC system overvoltage problem.

2. Topology and Basic Control of Offshore Wind Power Transmission via Diode Rectifier Units

2.1. System Topology

The topology of the offshore wind power transmission system via diode rectifier units is shown in Figure 1. The offshore wind farm is collected via the collector cable system to the point of common coupling (PCC), which is then connected to the sending-end DRU. The DRU rectifies the AC power output from the wind farm into DC power, which is transmitted through the DC submarine cable to the onshore receiving-end converter station; the receiving-end converter station adopts a hybrid MMC. Since the DRU cannot actively build up voltage, the wind turbines must establish and maintain the offshore AC voltage and frequency through grid-forming control, while the receiving-end converter station is mainly responsible for DC voltage control.

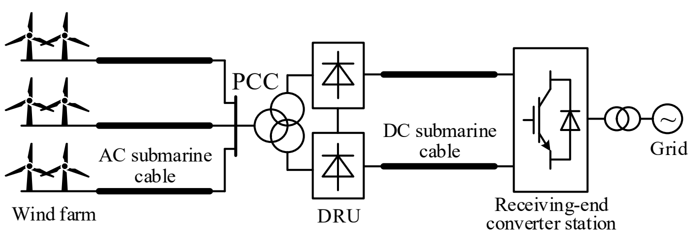

Figure 1. Topology of offshore wind power transmission via diode rectifier units.

2.2. Wind Turbine Control Strategy

The wind farm adopts direct-drive permanent magnet synchronous wind turbines, mainly composed of a machine-side converter and a grid-side converter. The machine-side converter maintains the wind turbine's DC bus voltage, while the grid-side converter controls the offshore AC voltage and frequency. Because the active power output of the wind turbine is strongly correlated with the sending-end AC voltage magnitude, and the reactive power output with the sending-end AC frequency [18], P/V and Q/f outer loops are adopted in the grid-side converter control, with voltage and current inner loops providing fast current regulation and voltage source characteristics. The complete control structure is shown in Figure 2.

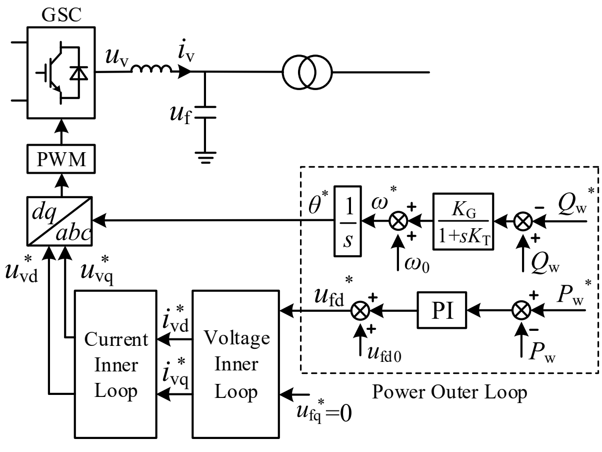

Figure 2. Control strategy of the wind turbine grid-side converter.

2.3. Receiving-End Converter Station Control Strategy

The receiving-end converter station maintains the voltage stability of the DC transmission line, and inverts the wind power transmitted via the DC line before feeding it into the receiving-end AC grid. A hybrid MMC is adopted for its larger DC voltage regulation range and its capability of DC fault current blocking and voltage step-down operation, which improves the fault ride-through capability under complex conditions [19,20]. As shown in Figure 3, the control strategy includes submodule capacitor voltage control, reactive power control, and DC voltage control, which generate the d-axis current reference, the q-axis current reference, and the DC current inner loop reference, respectively.

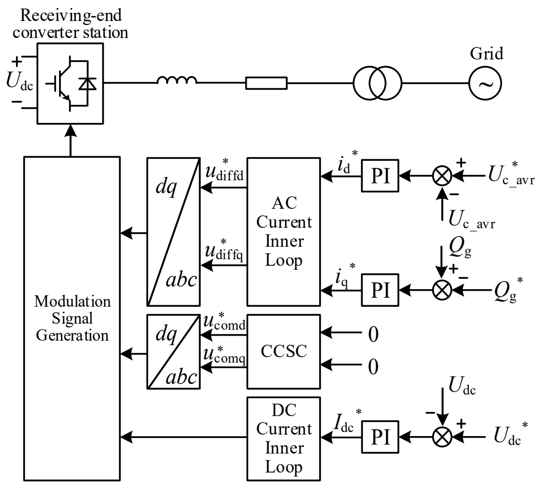

Figure 3. Control strategy of the receiving-end converter station.

3. Sending-End AC Fault Characteristic Analysis and Fault Ride-Through Strategy

3.1. Transient Characteristics Under the Traditional Wind-Turbine Current-Limiting Fault Ride-Through Strategy

According to the technical requirements for wind farm grid integration, once the voltage at the wind farm's point of common coupling U_{pcc} drops to 0.8 p.u., the grid-side converter of each wind turbine switches from its normal steady-state control to a low-voltage ride-through control mode, in which the outer power control is replaced by direct current-loop regulation and the wind turbine is required to inject reactive current into the grid. The corresponding d-axis and q-axis current references are given by

$$\begin{cases} i_{\mathrm{vq}}^{*} = K \times (0.9 - U_{\mathrm{pcc}}) \times I_{\mathrm{wN}} \\ i_{\mathrm{vd}}^{*} = \sqrt{I_{\mathrm{wmax}}^{2} - i_{\mathrm{vq}}^{2}} \end{cases} \quad (0 \leq U_{\mathrm{pcc}} \leq 0.9) \tag{1}$$

where K is the proportional coefficient of the dynamic reactive current, I_{wmax} is the maximum output current of the wind turbine, and I_{wN} is the rated current of the wind turbine.

In the traditional fault ride-through strategy based on wind-turbine current limiting, the receiving-end converter station maintains the DC voltage at its rated value during the fault, and the transient process is shown in Figure 4. The DRU output DC voltage $U_{\mathrm{dc,DRU}}$ is jointly determined by U_{pcc} and the DC current I_{dc}, and can be expressed as:

$$U_{\mathrm{dc,DRU}} = K_{\mathrm{d}} U_{\mathrm{pcc}} - X_{\mathrm{d}} I_{\mathrm{dc}} \tag{2}$$

where $K_{\mathrm{d}} = 6\sqrt{2}K_{\mathrm{T}}/\pi$, $X_{\mathrm{d}} = 6X_{\mathrm{T}}/\pi$ and K_{T} and X_{T} are the transformation ratio and leakage reactance of the converter transformer, respectively. When the voltage drop fault occurs in the sending-end AC system, the AC line-voltage magnitude U_l drops rapidly. According to Equation (2), the drop in AC voltage at the sending end will directly lead to a decrease in DRU output DC voltage. The direct current expression is:

$$I_{\mathrm{dc}} = \frac{U_{\mathrm{dc,DRU}} - U_{\mathrm{dc}}}{R_{\mathrm{dc}}} \tag{3}$$

where R_{dc} is the resistance of the DC line. When the DRU output DC voltage $U_{\mathrm{dc,DRU}}$ is less than or equal to the receiving-end DC voltage U_{dc}, the DC current rapidly drops to zero, causing the DRU to block. At this point, the DRU can no longer rectify normally; the active power of the wind farm can no longer be transmitted outward, and, in severe cases, the wind turbine or converter-station protection may trip, causing the system to shut down and disconnect from the grid. Therefore, relying solely on the traditional wind-turbine current-limiting fault ride-through strategy is inadequate for sending-end AC voltage drop faults, and a fault ride-through strategy more suitable for sending-end AC faults in DRU-HVDC systems needs to be designed.

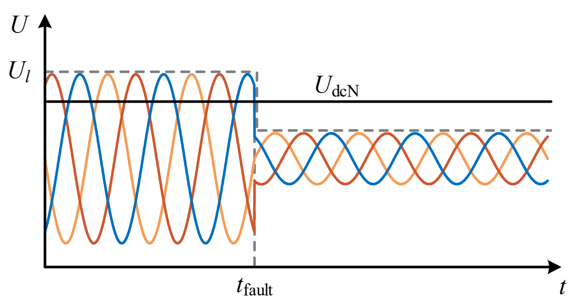

Figure 4. Transient process of AC fault at the sending end under traditional fault ride-through strategy.

3.2. Analysis of DC System Active Power Characteristics

Combining Equations (2) and (3), the relationship between the receiving-end DC voltage U_{dc} and the sending-end AC voltage U_{pcc} and the DC current I_{dc} can be obtained as:

$$U_{dc} = K_d U_{pcc} - (X_d + R_{dc}) I_{dc} \quad (4)$$

Furthermore, the functional relationship between the DC system's transmitted active power P_{dc} and I_{dc} can be obtained:

$$P_{dc} = U_{dc} I_{dc} = K_d U_{pcc} I_{dc} - (X_d + R_{dc}) I_{dc}^2 \quad (5)$$

After a sending-end AC fault occurs, U_{pcc} drops to $U_{pcc,f}$. In order to keep the DRU conducting, U_{dc} cannot remain at a fixed value and must be reduced accordingly. Assuming the DRU remains conducting during the fault, P_{dc} and I_{dc} still satisfy the relationship in Equation (5), and for any operating point, a U_{dc} value satisfying the DRU conduction condition can be determined. Equation (5) expresses P_{dc} as a function of I_{dc}, which is a downward-opening parabola with zeros at $I_{dc} = 0$ and $I_{dc} = K_d U_{pcc,f}/(X_d + R_{dc})$. Therefore, without considering other constraints, the range of I_{dc} corresponding to $P_{dc} \geq 0$ is:

$$0 \leq I_{dc} \leq \frac{K_d U_{pcc,f}}{X_d + R_{dc}} \quad (6)$$

and at the symmetry axis

$$I_{dc,sym} = \frac{K_d U_{pcc,f}}{2(X_d + R_{dc})} \quad (7)$$

P_{dc} reaches its theoretical maximum value:

$$P_{dc,max}^0 = \frac{(K_d U_{pcc,f})^2}{4(X_d + R_{dc})} \quad (8)$$

In addition, during the fault, the DC current is also limited by the allowable current of the DRU, the converter transformer, the DC line, and the receiving-end converter station. Defining $I_{dc,max}$ as the maximum current allowed by the DC system, and considering the DC current limit, the range of I_{dc} corresponding to $P_{dc} \geq 0$ becomes:

$$0 \leq I_{dc} \leq I_{dc,lim} \quad (9)$$

where

$$I_{dc,lim} = \min\left[I_{dc,max}, \frac{K_d U_{pcc,f}}{X_d + R_{dc}}\right] \quad (10)$$

3.3. Sending-End Fault Ride-Through Strategy Based on Active Voltage Reduction of the Receiving-End Converter Station

To solve the problem of DRU blocking caused by an AC fault at the sending end under the traditional fault ride-through strategy, a fault ride-through strategy based on active voltage reduction of the receiving-end converter station is proposed in this paper.

Based on the analysis results in Section 3.2, an active voltage reduction control loop based on the DC current deviation is added to the original DC voltage control loop of the receiving-end converter station, as shown in Figure 5a. It enables U_{dc} to changes from a fixed value to a variable that adaptively adjusts with the fault severity during a sending-end fault, so that the operating point of the DC system is maintained within the feasible region. The control loop takes the deviation between the active voltage reduction threshold I_{dc}^* and the actual DC current I_{dc} as its input, generates the DC voltage correction ΔU through the

PI controller, and superimposes it on the rated DC voltage U_{dcN} to form the DC voltage reference value U_{dc}^{*} during the fault. Its control law is:

$$\begin{cases} \Delta U = (k_{ip} + \frac{k_{ii}}{s})(I_{dc} - I_{dc}^{*}) \\ U_{dc}^{*} = \Delta U + U_{dcN} \end{cases} \tag{11}$$

The setting of I_{dc}^{*} is considered for two cases: an online value calculated during the fault, and a preset value used under steady-state operation. During the fault, I_{dc} must not exceed the upper limit given by Equation (10). It requires U_{pcc} to be measured and transmitted to the receiving-end converter station, where $I_{dc,lim}$ is calculated online to determine the specific value of I_{dc}. However, the measurement and communication of U_{pcc} involve time delays. Therefore, an I_{dc}^{*} is preset in the steady state, so that the active voltage reduction control loop can respond quickly at the onset of a fault, thus preventing the DRU from blocking.

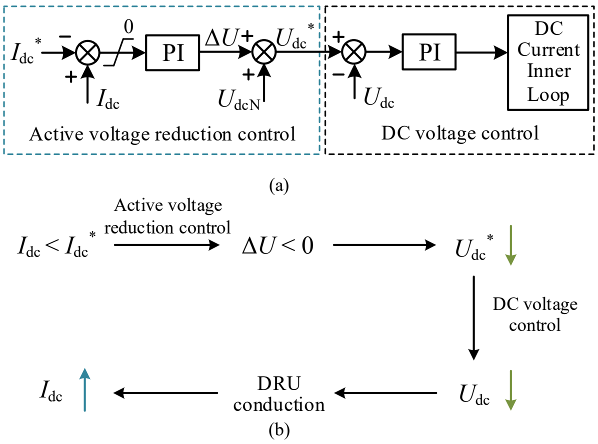

Figure 5. Active voltage reduction fault ride-through strategy of the receiving-end converter station and its mechanism: (**a**) active voltage reduction fault ride-through strategy; (**b**) operating mechanism during the fault.

3.3.1. Online Calculation Value During the Fault

After the measured value of U_{pcc} converges and stabilizes, the controller calculates the corresponding $I_{dc,lim}$ from Equation (10). To transmit as much active power as possible, a margin coefficient $k_m \in (0, 1]$ is introduced. When $I_{dc,max} > I_{dc,sym}$, I_{dc}^{*} is set as:

$$I_{dc}^{*} = k_m I_{dc,sym} \tag{12}$$

The $I_{dc,sym}$ already lies within the maximum current allowed by the system. So k_m can be set to 1 to make P_{dc} as large as possible.

When $I_{dc,max} \leq I_{dc,sym}$, I_{dc}^{*} is set as:

$$I_{dc}^{*} = k_m I_{dc,max} \tag{13}$$

The theoretical optimal operating point exceeds the system's allowable maximum current $I_{dc,max}$; k_m must be set to a value less than 1, mainly to leave a margin between the actual value of I_{dc}^{*} and $I_{dc,max}$, preventing I_{dc} from exceeding $I_{dc,max}$ and thereby improving the safety of the control. In practice, the value of km can be chosen empirically, set as close to 1 as safety allows, so as to transmit as much active power as possible.

3.3.2. Steady-State Preset Value

In order to enable the active voltage reduction control loop to respond quickly during the period from the occurrence of a fault to obtaining the online calculation value, a steady-state threshold I_{dc0} is preset under normal operating conditions. The threshold serves as the steady-state reference value I_{dc}^{*}.

Considering a relatively severe fault condition, with $U_{pcc,f}$ = 0.1 p.u. taken as the preset fault severity. Based on the specific system parameters, the relationship between $I_{dc,max}$ and $I_{dc,sym}$ is determined, and the corresponding equation, Equation (12) or Equation (13), is used to compute the steady-state threshold offline in advance.

The output of the DC current comparator in the active voltage reduction control loop is limited to an upper bound of zero. Under normal operating conditions, the limiter blocks the threshold from taking effect, so the original constant DC voltage control of the receiving-end converter station is not affected:

$$\begin{cases} \Delta U < 0, \ I_{dc} < I_{dc}^{*} \\ \Delta U = 0, \ I_{dc} \geq I_{dc}^{*} \end{cases} \tag{14}$$

The combination of the preset threshold and the limiter prevents the active voltage reduction control from being triggered by mistake during normal operation. At the same time, it allows the control to engage automatically when the DC current drops due to a fault at the sending end, without requiring additional fault detection.

The operating mechanism of the active voltage reduction fault ride-through strategy is shown in Figure 5b. After the fault occurs, the DC current I_{dc} falls below the threshold I_{dc}^{*}, and the active voltage reduction control loop is activated. Based on the DC current deviation, the loop generates a negative voltage correction ΔU. The correction is added to the rated DC voltage reference, reducing the DC voltage reference value U_{dc}^{*} of the receiving-end converter station. The DC voltage control loop then drives the actual DC voltage U_{dc} to follow this lower reference. As the DC voltage decreases, the DRU again satisfies its conduction condition. The DC current I_{dc} recovers, and the active power P_{dc} increases accordingly.

The proposed active voltage reduction strategy also has a theoretical operating limit. In the extreme case of a metallic three-phase fault at the sending end, where U_{pcc} collapses completely to zero, the DRU output DC voltage $U_{dc,DRU}$ likewise falls to zero. If the active voltage reduction control loop continued to command a nonzero DC current under this condition, the resulting DC voltage reference U_{dc} would be driven negative, which is not physically meaningful and could cause the submodule capacitors of the receiving-end converter station to charge rapidly, potentially resulting in a loss of control. To address the limiting condition, a lower bound of zero is imposed on the DC voltage reference U_{dc} in the receiving-end converter station's control loop, preventing U_{dc}^{*} from becoming negative.

4. Receiving-End AC Fault Characteristic Analysis and Fault Ride-Through Strategy

4.1. Transient Characteristics Under the Traditional DC Energy Dissipation Fault Ride-Through Strategy

When a fault occurs in the receiving-end AC grid, the voltage at the fault point drops instantaneously, and the active power output of the receiving-end converter station is hindered. DRU does not have power regulation capability, and the output active power of the wind farm continues to be injected into the DC system. This leads to a large amount of active power surplus in the DC system, forcing the sub-module capacitor of the receiving-end converter station to charge quickly. Due to the lack of effective energy dissipation channels in the DC system, the DC bus voltage will soon exceed the relay protection action limit. In severe cases, it will trigger the blocking of the converter station, which will cause the system to stop running and seriously threaten the safe and stable operation of the system.

To address this problem, existing studies mostly adopt a DC chopper connected in parallel on the DC side of the receiving-end converter station to achieve fault ride-through, as shown in Figure 6. The DC chopper is composed of a power switch, such as an IGBT, and a crowbar resistor, which are connected in series and then connected to the DC bus. During normal operation, the device remains blocked and does not participate in operation; when the DC voltage exceeds the upper threshold U_H, the switching device conducts, converting the surplus energy into heat to suppress the DC overvoltage; when the voltage falls back to the lower threshold U_L, the switch turns off and the energy-dissipation branch is withdrawn.

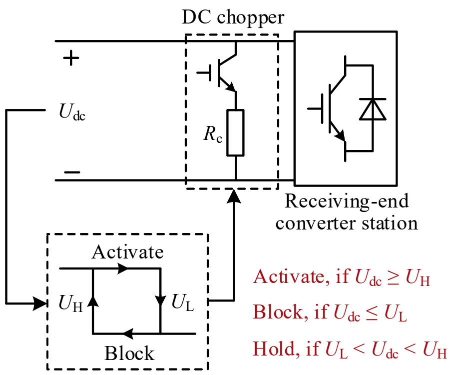

Figure 6. Traditional DC energy dissipation fault ride-through strategy.

Under the traditional DC energy dissipation strategy, the sending-end AC voltage U_{pcc} exhibits pronounced periodic oscillation during the fault. The reason is that the repeated switching of the chopper causes the DC voltage U_{dc} to oscillate periodically between U_H and U_L. In the MMC-HVDC system, if the DC chopper is likewise adopted at the receiving end, this periodic fluctuation of U_{dc} generally remains confined to the DC side. Because the sending-end converter station is itself a fully controllable MMC that actively establishes the sending-end AC voltage through its own grid-forming control, consisting of a V/f outer loop and voltage and current double inner loops. Therefore, the AC-side voltage is generated independently of the instantaneous DC bus voltage. The DRU cannot isolate the DC-side voltage oscillation, which is further transmitted to the AC bus at the sending end, causing the AC voltage to fluctuate repeatedly. As shown in Figure 7, the waveforms of U_{pcc} and U_{dc} are nearly identical in shape and oscillation frequency, which directly reflects this transmission mechanism.

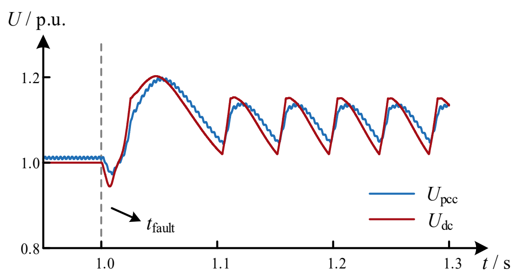

Figure 7. Schematic diagram of voltage fluctuation under the traditional DC energy dissipation strategy.

The oscillation has several adverse effects. First, the repeated voltage impacts increase the voltage stress on the DC line and the converter, accelerating component fatigue. Second, the sustained AC voltage disturbance interferes with the normal operation of the wind turbine control system, creating a risk of turbine disconnection. Third, the resistive dissipation process is limited by the switching response speed and the energy dissipation rate, making it difficult to promptly consume the surplus power that accumulates rapidly at the onset of the fault. As a result, the suppression of the initial DC overvoltage peak is limited. These issues motivate the design of a receiving-end AC fault ride-through strategy that better matches the topology and operating characteristics of the DRU-HVDC system.

4.2. Analysis of the Coupling Relationship Between Wind Turbine Outlet Voltage and DC Voltage

During a receiving-end AC fault, the DC bus voltage keeps rising mainly because the active power generated by the wind farm and delivered to the DC system exceeds the active power that the MMC can transmit to the receiving-end grid. However, the wind farm is located offshore. Without a communication link, the wind farm cannot directly obtain the real-time value of U_{dc}. This section therefore establishes the relationship between the wind turbine outlet voltage U_{f} and the DC voltage U_{dc}, which provides a circuit-level basis for the fault ride-through strategy proposed later.

The derivation in this section is based on two approximations. First, in offshore wind power transmission systems, the resistances of AC collector cables and DC transmission lines are typically on the order of a few hundredths of an ohm per kilometer. For representative line lengths and rated power levels, the resulting active-power losses and voltage drops are relatively small. Therefore, the active-power losses and voltage drops caused by the resistances of the AC collector cables and DC transmission line are neglected in the simplified derivation. Second, the transformation ratios of the wind turbine step-up transformers and the offshore substation transformers are assumed to remain constant.

From Equation (4):

$$U_{\mathrm{pcc}} = \frac{1}{K_{\mathrm{d}}}[U_{\mathrm{dc}} + (R_{\mathrm{dc}} + X_{\mathrm{d}})I_{\mathrm{dc}}] \tag{15}$$

According to the approximate conditions, the active power of the wind farm can be considered approximately equal to the active power delivered to the receiving end:

$$\sum_{j=1}^{n} P_{\mathrm{w}j} \approx P_{\mathrm{dc}} = U_{\mathrm{dc}} I_{\mathrm{dc}} \tag{16}$$

where n is the number of wind farms, j is the wind farm index, $P_{\mathrm{w}j}$ is the active power output by wind field j.

Combining Equations (15) and (16) to eliminate I_{dc} gives:

$$U_{\mathrm{pcc}} = \frac{1}{K_{\mathrm{d}}}\left[U_{\mathrm{dc}} + (R_{\mathrm{dc}} + X_{\mathrm{d}})\frac{\sum\limits_{j=1}^{n} P_{\mathrm{w}j}}{U_{\mathrm{dc}}}\right] \tag{17}$$

A wind turbine step-up transformer and an offshore substation transformer separate the wind turbine grid-side converter from the offshore PCC. As a result, U_{f} and U_{pcc} differ in magnitude, but their ratio is constant. Let $K_{\mathrm{w}} = U_{\mathrm{pccN}}/U_{\mathrm{fN}}$ denote this combined transformation ratio, then U_{pcc} can be expressed as $U_{\mathrm{pcc}} \approx K_{\mathrm{w}} U_{\mathrm{f}}$. Substituting the relation into Equation (17) gives the relationship between U_{f} and U_{dc}:

$$U_{\mathrm{f}} = \frac{1}{K_{\mathrm{w}} K_{\mathrm{d}}}\left[U_{\mathrm{dc}} + (R_{\mathrm{dc}} + X_{\mathrm{d}})\frac{\sum\limits_{j=1}^{n} P_{\mathrm{w}j}}{U_{\mathrm{dc}}}\right] \tag{18}$$

Differentiating Equation (18) with respect to U_{dc} gives:

$$\frac{\partial U_{\mathrm{f}}}{\partial U_{\mathrm{dc}}}=\frac{1}{K_{\mathrm{w}}K_{\mathrm{d}}}\left[1-\frac{(R_{\mathrm{dc}}+X_{\mathrm{d}})\sum\limits_{j=1}^{n}P_{\mathrm{w}j}}{U_{\mathrm{dc}}^{2}}\right] \tag{19}$$

This derivative is zero at:

$$U_{\mathrm{dc,sym}}=\sqrt{(R_{\mathrm{dc}}+X_{\mathrm{d}})\sum_{j=1}^{n}P_{\mathrm{w}j}} \tag{20}$$

which corresponds to the minimum point of the curve described by Equation (18). Assuming the wind turbine maintains its rated active power output, $\Sigma P_{\mathrm{w}j}\approx U_{\mathrm{dcN}}I_{\mathrm{dcN}}$ in Equation (20), giving:

$$U_{\mathrm{dc,sym}}=\sqrt{(R_{\mathrm{dc}}+X_{\mathrm{d}})U_{\mathrm{dcN}}I_{\mathrm{dcN}}}=\sqrt{\alpha}U_{\mathrm{dcN}} \tag{21}$$

where

$$\alpha=\frac{(R_{\mathrm{dc}}+X_{\mathrm{d}})I_{\mathrm{dcN}}}{U_{\mathrm{dcN}}} \tag{22}$$

The numerator of α represents the voltage drop produced by the equivalent impedance of the converter transformer and the DC line at rated current. This value is much smaller than the denominator, U_{dcN}. Therefore, $0<\alpha<1$, and Equation (21) shows that $U_{\mathrm{dc,sym}}<U_{\mathrm{dcN}}$.

Consequently, within the operating range $U_{\mathrm{dc}}>U_{\mathrm{dcN}}$, the derivative in Equation (19) is always positive, and U_{f} increases monotonically with U_{dc}. In other words, when a receiving-end AC fault causes U_{dc} to rise, this rise is reflected as a corresponding monotonic increase in the wind turbine outlet voltage U_{f}. Furthermore, based on Equation (18), the wind turbine can indirectly sense the degree to which the receiving-end DC bus voltage exceeds its limit by monitoring this local quantity.

4.3. Receiving-End Fault Ride-Through Strategy Based on Source-Side Active Power Reduction

To solve the DC overvoltage problem during a receiving-end AC fault, a receiving-end fault ride-through strategy based on source-side active power reduction is proposed in this paper, shown in Figure 8a. This strategy makes use of the monotonic relationship between U_{f} and U_{dc} established in Section 4.2.

An active power reduction control loop is added before the active power outer loop of the grid-forming control at the grid-side converter. The loop uses U_{f} to represent the degree of power imbalance in the DC system. In this way, information about the receiving-end fault is mapped to the wind turbine control layer.

The input to this control loop is the deviation between the grid-side converter outlet voltage threshold U_{f}^{*} and the actual value U_{f}. A PI controller converts this deviation into an active power correction ΔP, which is added to the wind turbine MPPT command $P_{\mathrm{w,MPPT}}$ to form the active power reference value P_{w}^{*} during the fault:

$$\begin{cases}\Delta P=(k_{\mathrm{up}}+\frac{k_{\mathrm{ui}}}{s})(U_{\mathrm{f}}^{*}-U_{\mathrm{f}})\\ P_{\mathrm{w}}^{*}=\Delta P+P_{\mathrm{w,MPPT}}\end{cases} \tag{23}$$

In the DC system, the upper limit of the DC voltage and the submodule capacitor voltage is generally set to 1.3 p.u. [21]. From Equation (18), when U_{dc} reaches this upper limit of 1.3 p.u., the corresponding outlet voltage level is:

$$U_{\mathrm{f,lim}} = \frac{1}{K_{\mathrm{w}}K_{\mathrm{d}}}\left[1.3U_{\mathrm{dcN}} + (R_{\mathrm{dc}} + X_{\mathrm{d}})\frac{\sum\limits_{j=1}^{n} P_{\mathrm{w}j}}{1.3U_{\mathrm{dcN}}}\right] \tag{24}$$

Introducing a margin coefficient $k_{\mathrm{n}} \in (0, 1)$ gives the voltage threshold adopted by the active power reduction control loop:

$$U_{\mathrm{f}}^{*} = U_{\mathrm{fN}} + k_{\mathrm{n}}(U_{\mathrm{f,lim}} - U_{\mathrm{fN}}) \tag{25}$$

During normal operation, U_{f} remains close to U_{fN}, while $U_{\mathrm{f,lim}}$ is higher than U_{fN}. The k_{n} is used to quantify the gap between U_{fN} and $U_{\mathrm{f,lim}}$. The value of k_{n} must balance two considerations. First, k_{n} cannot be set to 1. If $k_{\mathrm{n}} = 1$, then $U_{\mathrm{f}}^{*} = U_{\mathrm{f,lim}}$, which would mean the active power reduction control loop only acts after U_{f} has already exceeded its limit. It is unsuitable. In addition, according to Reference [22] in the manuscript, U_{f} generally does not exceed 1.05 p.u. during normal operation. Therefore, k_{n} should be chosen such that U_{f}^{*} is not lower than 1.05 p.u. Therefore, the value of k_{n} should be determined based on the specific system and the desired DC voltage level during a receiving-end fault.

It should be noted that $U_{\mathrm{f,lim}}$ in Equation (24), and the threshold U_{f}^{*} obtained from Equation (25), depend on the aggregate active power of all the wind farms, as well as the system-level parameters (K_{w}, K_{d}, R_{dc}, X_{d}, U_{dcN}) that are identical throughout the system. Consequently, every wind turbine computes the same value of $U_{\mathrm{f,lim}}$ and U_{f}^{*} using the same formula and the same inputs.

The output of the voltage comparator in the active power reduction control loop is limited to an upper bound of zero. This ensures that the control loop acts only when the outlet voltage U_{f} exceeds the threshold, and it does not alter the original power command under normal operation:

$$\begin{cases} \Delta P < 0,\ U_{\mathrm{f}} > U_{\mathrm{f}}^{*} \\ \Delta P = 0,\ U_{\mathrm{f}} \leq U_{\mathrm{f}}^{*} \end{cases} \tag{26}$$

The operating mechanism of the source-side active power reduction fault ride-through strategy is shown in Figure 8b. After a receiving-end AC fault occurs, the RMS value of the wind turbine outlet voltage U_{f} rises. The active power reduction control loop detects that $U_{\mathrm{f}}^{*} < U_{\mathrm{f}}$ and outputs a negative active power correction ΔP. The active power reference value P_{w}^{*} of the wind turbine is then actively reduced. The wind turbine correspondingly reduces its active power output, so the active power injected into the DC system decreases. It suppresses the DC-side power surplus, restrains the rising trend of U_{dc}, and gradually stabilizes the system, forming a complete regulation loop.

The proposed source-side active power reduction strategy has a corresponding theoretical operating limit. In the extreme case where the receiving-end AC voltage collapses completely to zero, the active power that the receiving-end converter station can deliver to the grid is likewise forced to zero. To maintain the active-power balance between the input and output of the receiving-end converter station, the active power injected by the wind farm would also need to be reduced to zero, causing a significant disturbance to the wind farm's own operation. It represents a theoretical operating limit of the proposed strategy. In practical systems, however, the receiving-end AC network is generally a regional grid, and a complete collapse of its voltage to zero is not a realistic operating condition.

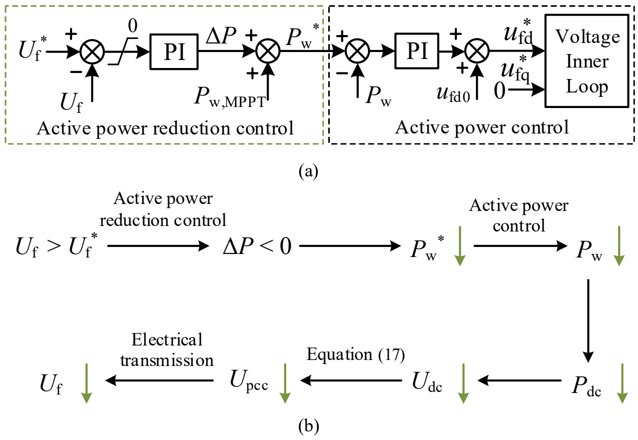

Figure 8. Source-side active power reduction fault ride-through strategy and its mechanism: (**a**) source-side active power reduction fault ride-through strategy; (**b**) operating mechanism during the fault.

5. Simulation Verification

To verify the effectiveness of the proposed fault ride-through strategies, a simulation model of the DRU-HVDC transmission system shown in Figure 1 was built in PSCAD/EMTDC. In the model, each wind farm is represented by a single equivalent generator wind turbine, and its rated capacity is equal to the total installed capacity of the corresponding wind farm, which is 300 MW, 400 MW, and 400 MW, respectively. The equivalent generator is obtained by aggregating the individual wind turbines within the wind farm using the classical method of Reference [23]. The receiving-end inverter station adopts a hybrid MMC. The receiving-end AC system is represented by a 500 kV voltage source. The main system parameters are listed in Table 1. The PI parameters and their setting methods are shown in Appendix A.

Table 1. Main parameters of the simulation system.

Equipment	Parameter	Value
Wind farms	Rated power/MW	300(#1), 400(#2), 400(#3)
	Frequency/Hz	50
	Transformer ratio	0.69 kV/35 kV
Offshore substation	Rated capacity/MV·A	300(#1), 400(#2), 400(#3)
	Transformer ratio	35 kV/220 kV
DRU	Rated capacity/MV·A	1100
	Transformer ratio	220 kV/300 kV
	Transformer leakage inductance/mH	20
DC line	Length/km	100
	Resistance per unit length/($\Omega\cdot$km^{-1})	0.01
	Inductance per unit length/(mH·km^{-1})	0.90
	Capacitance per unit length/(uF·km^{-1})	0.013
Receiving-end converter station	Rated capacity/MV·A	1100
	Transformer ratio	500 kV/416.41 kV
	Rated DC voltage/kV	800
	Number of submodules per arm	400
	Rated submodule voltage/kV	2
	Submodule capacitance/uF	9000
	Arm reactor/mH	133

Based on this simulation model, sending-end and receiving-end AC fault scenarios were set up separately. The transient responses of the system under the traditional fault ride-through strategy and under the proposed strategy are compared and analyzed. Specifically, the wind-turbine current-limiting strategy described in Section 3.1 is adopted as the traditional method for sending-end AC faults, and the DC chopper-based DC energy dissipation strategy described in Section 4.1 is adopted as the traditional method for receiving-end AC faults, each compared against the corresponding strategy proposed in this paper.

5.1. Sending-End AC Fault Simulation Results

5.1.1. Sending-End Three-Phase AC Voltage Drop Fault

(1) Fault duration 300 ms, voltage drop 50%

At simulation time t = 0.5 s, a symmetrical three-phase voltage sag was applied at the sending end, lasting 300 ms before being cleared. During the fault, U_{pcc} dropped by 50%. In the proposed active voltage reduction fault ride-through strategy, $I_{dc,max}$ was set to the rated DC current of the receiving-end converter station, 1.375 kA. Calculations showed that $I_{dc,sym}$ exceeds $I_{dc,max}$ under this fault condition. Therefore, I^*_{dc} was calculated using Equation (13), with a margin coefficient k_m = 0.85, giving $I^*_{dc} \approx 1.16$ kA. The steady-state preset threshold I_{dc0} of the active voltage reduction control loop was also calculated to be 1.16 kA. The response waveforms of the system under the proposed strategy and under the traditional current-limiting strategy are compared in Figure 9.

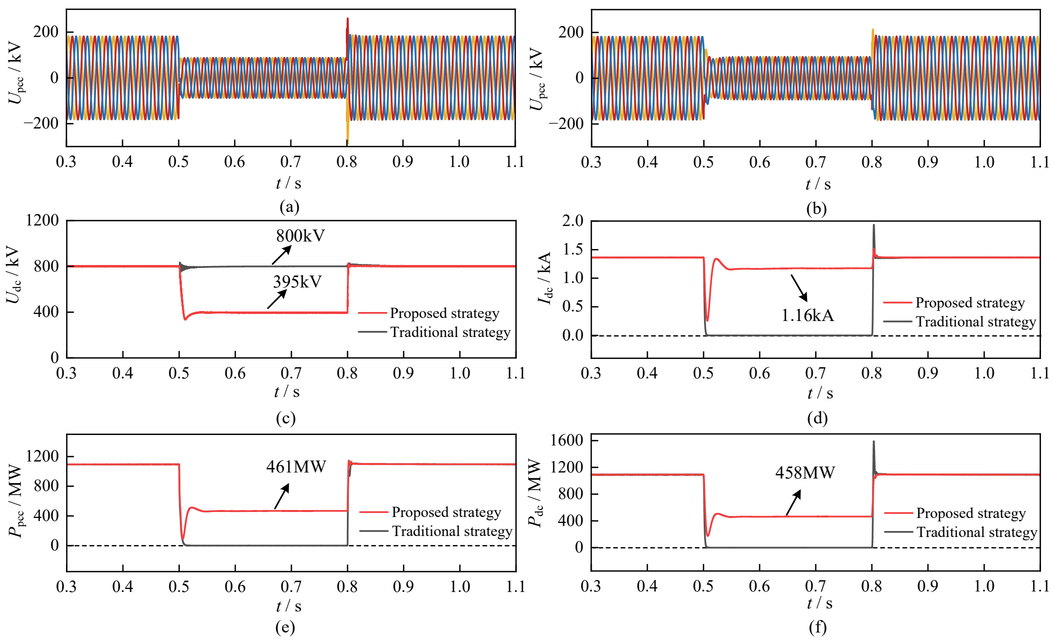

Figure 9. Simulation results of sending-end AC fault: fault duration 300 ms, voltage drop 50%: (**a**) sending-end AC voltage U_{pcc} under the traditional strategy; (**b**) sending-end AC voltage U_{pcc} under the proposed strategy; (**c**) DC voltage U_{dc}; (**d**) DC current I_{dc}; (**e**) sending-end active power P_{pcc}; (**f**) receiving-end active power P_{dc}.

Figure 9 shows that, under the traditional strategy, the receiving-end converter station keeps the DC voltage at its rated value of 800 kV throughout the fault. After the sending-end AC fault occurs, the RMS sending-end AC voltage drops rapidly, while the DC-side voltage remains at a relatively high level. This causes the DRU to lose its conduction condition and enter the blocking state. As a result, the DC current drops rapidly to zero during the fault, both the sending-end and receiving-end active power are interrupted, and the wind farm output can no longer be delivered through the DC line. Although the system restores power transmission after the fault is cleared, the DC power path is completely blocked while the fault is present.

In contrast, under the proposed active voltage reduction strategy, the drop in sending-end voltage causes the DC current to fall, which automatically activates the active voltage reduction control loop. The loop lowers the DC voltage reference value, reducing the DC voltage from about 800 kV to about 395 kV. With the lower DC voltage, the DRU again satisfies its conduction condition. During the fault, the DC current is maintained at about 1.16 kA, and the receiving-end active power stabilizes at about 458 MW. These results show that the proposed strategy maintains active power transmission during a sending-end AC voltage drop, avoiding the power interruption caused by DRU blocking under the traditional strategy.

After the fault is cleared, the sending-end AC voltage U_{pcc} recovers to its rated value in a step change. According to Equation (2), the DRU output DC voltage $U_{\mathrm{dc,DRU}}$ rises accordingly. According to Equation (3), the DC current I_{dc} rises rapidly as well. Once I_{dc} recovers above the threshold I_{dc}^{*}, the comparator output is clamped to zero by the limiter logic, so the voltage correction ΔU converges continuously to zero and the DC voltage reference U_{dc}^{*} smoothly returns to its rated value U_{dcN}, at which point the active voltage reduction control loop is deactivated. The control law itself involves no discrete jump, and therefore there is no risk of the control loop being repeatedly re-triggered.

Table 2 further summarizes the comparison using measurable indicators, including the maximum DC-voltage deviation, the minimum DC current, the transmitted active power during the fault, the recovery time and overshoot after fault clearance, and the maximum power loss relative to the rated capacity.

Table 2. Comparison of sending-end AC fault ride-through performance.

Indicator	Proposed Strategy	Traditional Strategy
Maximum U_{dc} deviation during the fault	405 kV	0 kV
Minimum I_{dc} during the fault	1.16 kA	0 kA (DRU blocked)
P_{dc} during the fault	458 MW	0 MW
Maximum power loss (relative to rated capacity)	58%	100%
Recovery of U_{dc}	Overshoot $\approx$ 7.5% ($\approx$60 kV); recovery time $\approx$ 15 ms	—
Recovery of P_{dc}	Overshoot $\approx$ 6.5% ($\approx$70 MW); recovery time $\approx$ 25 ms	—

(2) Fault duration 200 ms, voltage drop 80%

At simulation time $t = 0.5$ s, a symmetrical three-phase voltage sag was applied at the sending end, lasting 200 ms before being cleared. During the fault, U_{pcc} dropped by 80%. Calculations showed that $I_{\mathrm{dc,sym}}$ exceeds $I_{\mathrm{dc,max}}$ under this fault condition. With the margin coefficient k_{m} set to 0.85, the calculated I_{dc}^{*} is 1.16 kA. The steady-state preset threshold I_{dc0} was also calculated to be 1.16 kA. The response waveforms of the system under the proposed strategy and under the traditional current-limiting strategy are compared in Figure 10.

Under the more severe condition, the traditional strategy still keeps the receiving-end DC voltage fixed at its rated value of 800 kV. Because the sending-end voltage collapse is now considerably deeper, the DRU loses its forward-conduction condition almost immediately, and the DC current and active power fall to zero throughout the fault, completely interrupting power transmission until the fault is cleared.

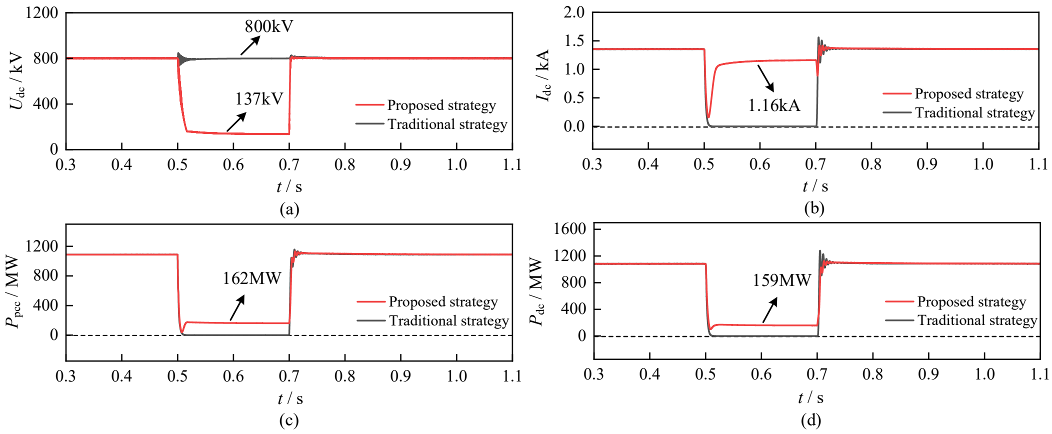

Figure 10. Simulation results of sending-end AC fault: fault duration 200 ms, voltage drop 80%: (**a**) DC voltage U_{dc}; (**b**) DC current I_{dc}; (**c**) sending-end active power P_{pcc}; (**d**) receiving-end active power P_{dc}.

Under the proposed strategy, the receiving-end DC voltage reference is again adaptively reduced according to the fault severity; because this fault is more severe, the reduction is also larger, with U_{dc} falling to about 137 kV, markedly lower than the reduction to about 395 kV observed under the 50%-sag case in Section 5.1.1(1). Despite this larger adjustment, the DC current is still maintained at about 1.16 kA, and the sending-end and receiving-end active power stabilize at about 162 MW and 159 MW, respectively. Although these power levels are lower than under the 50% fault, reflecting the reduced power-transfer capability available under a deeper sag, the DRU remains continuously conducting and power transmission is never interrupted. These results confirm that the proposed active voltage reduction strategy remains effective across different fault severities, consistently avoiding DRU blocking and maintaining continuous power transmission.

5.1.2. Sending-End Single-Line-to-Ground Fault

At simulation time t = 0.5 s, a single-line-to-ground fault was applied at the sending end, lasting 200 ms before being cleared. The response waveforms of the system under the two strategies are compared in Figure 11.

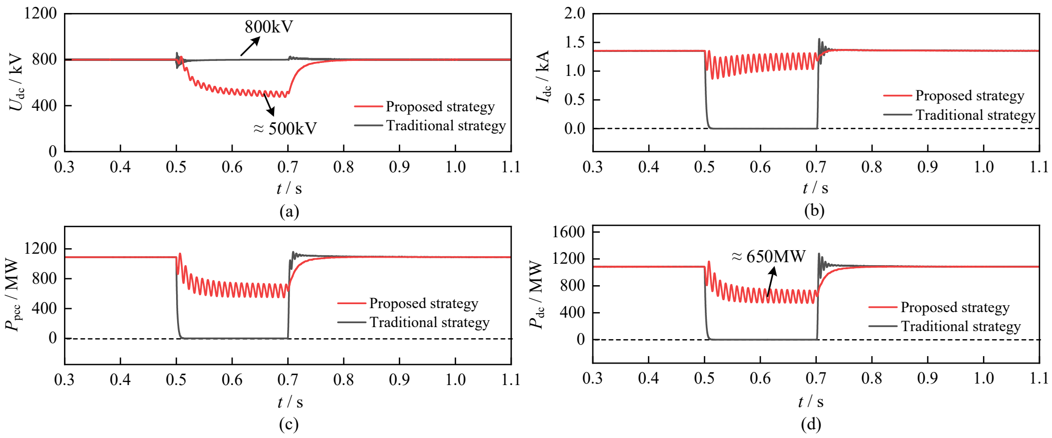

Figure 11. Simulation results of a sending-end single-line-to-ground fault: (**a**) DC voltage U_{dc}; (**b**) DC current I_{dc}; (**c**) sending-end active power P_{pcc}; (**d**) receiving-end active power P_{dc}.

Under the traditional strategy, because the receiving-end converter station keeps the DC voltage fixed at its rated value of 800 kV, the sending-end fault still causes the DRU to block and power transmission to be interrupted, consistent with the behavior observed under symmetrical faults. Under the proposed strategy, the receiving-end DC voltage is actively reduced and the DRU remains conducting. However, because the fault is asymmetrical, both the DC voltage and the DC current exhibit a pronounced second-harmonic ripple throughout the fault. It reveals a limitation of the proposed strategy: although the active voltage reduction control can keep the DRU conducting during an asymmetrical sending-end fault, the DRU itself has no controllable capability and therefore cannot isolate the double-frequency oscillation caused by the unbalanced fault, which is directly transmitted into the DC-side voltage and current.

5.1.3. Influence of System Parameter Variations on Sending-End Fault Ride-Through Strategy

According to Equations (7) and (8), the DC-line resistance R_{dc} and transformer leakage reactance X_d affect the theoretical maximum-power-point current $I_{dc,sym}$ and maximum transferable power $P^0_{dc,max}$ through the total equivalent impedance $X_d + R_{dc}$. When $I_{dc,max} > I_{dc,sym}$, Equation (12) applies, and the current reference $I^*_{dc} = k_m I_{dc,sym}$ varies directly with R_{dc} and X_d. When $I_{dc,max} \leq I_{dc,sym}$, Equation (13) applies and $I^*_{dc} = k_m I_{dc,max}$; in this regime, R_{dc} and X_d do not change the current reference as long as the inequality remains satisfied. Thus, parameter variations may change not only the theoretical maximum-power point but also the operating regime used to determine I^*_{dc}.

To evaluate this influence, an additional case is constructed based on the sending-end fault case in Section 5.1.1(2). The fault duration and voltage-sag depth are retained at 200 ms and 80%, respectively. Relative to the parameters in Table 1, R_{dc} is increased from 1 Ω to 9 Ω, and X_d is increased from 12 Ω to 54 Ω. Substitution into Equation (7) gives $I_{dc,sym} \approx 1.286$ kA, which is lower than $I_{dc,max} = 1.375$ kA. Therefore, Equation (12) applies. With $k_m = 1$, the calculated current reference is $I^*_{dc} \approx 1.286$ kA, and the corresponding DC voltage and transferred DC power are approximately 81.0 kV and 104.2 MW, respectively. The simulation results are shown in Figure 12.

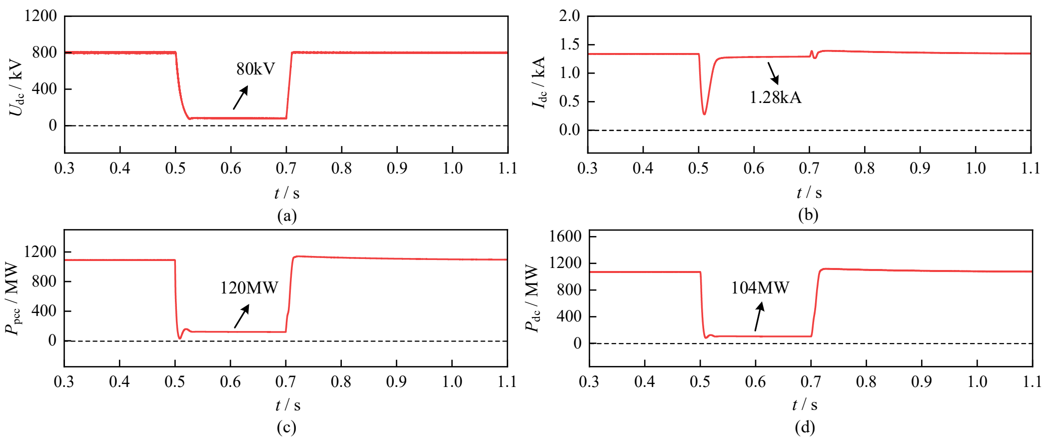

Figure 12. Simulation results under variations in R_{dc} and X_d during a sending-end AC fault: (**a**) DC voltage U_{dc}; (**b**) DC current I_{dc}; (**c**) sending-end active power P_{pcc}; (**d**) receiving-end active power P_{dc}.

As shown in Figure 12, after a brief transient at the fault onset, the DC voltage and DC current stabilize at approximately 80 kV and 1.28 kA, respectively, while the receiving-end DC power stabilizes at approximately 104 MW. These simulation results agree closely with the theoretical values of 81 kV, 1.286 kA, and 104.2 MW calculated above. The sending-end active power is approximately 120 MW, slightly higher than the receiving-end DC power because of the power losses associated with the increased equivalent impedance. The close agreement between the theoretical and simulated results verifies the parameter-dependent calculation of I^*_{dc} and confirms that the proposed strategy can maintain DRU conduction and continuous power transmission after substantial variations in R_{dc} and X_d.

5.2. Receiving-End AC Fault Simulation Results

5.2.1. Receiving-End Three-Phase AC Voltage Drop Fault

(1) Fault duration 300 ms, voltage drop 50%

At simulation time t = 0.5 s, a symmetrical three-phase voltage drop was applied at the receiving end, lasting 300 ms before being cleared. During the fault, the receiving-end AC voltage dropped by 50%. In the proposed source-side active power reduction strategy, the upper limit of the DC voltage was set to 1.3 p.u. Substituting this value into Equation (24) gives $U_{\mathrm{f,lim}} \approx 0.897$ kV (about 1.3 p.u.). The voltage threshold U_{f}^{*} was set to 1.05 p.u. (about 0.72 kV, corresponding to a margin coefficient k_{n} = 0.167). In the traditional DC energy dissipation strategy, the upper voltage threshold of the DC chopper was set to 1.05 p.u., which is 840 kV, and the lower threshold was set to 1 p.u. The response waveforms of the system under the two strategies during the fault are compared in Figure 13.

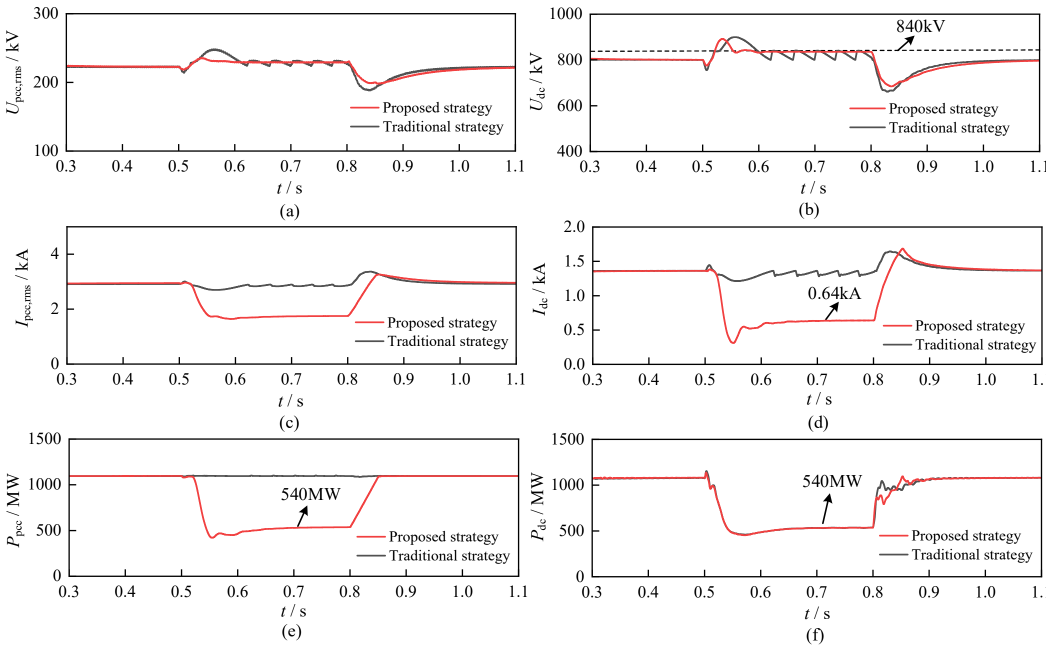

Figure 13. Simulation results of receiving-end AC fault: fault duration 300 ms, voltage drop 50%: (**a**) RMS sending-end AC voltage $U_{\mathrm{pcc,rms}}$; (**b**) DC voltage U_{dc}; (**c**) RMS sending-end AC current $I_{\mathrm{pcc,rms}}$; (**d**) DC current I_{dc}; (**e**) sending-end active power P_{pcc}; (**f**) receiving-end active power P_{dc}.

After the three-phase voltage drop occurs at the receiving end, the ability of the receiving-end converter station to deliver active power to the grid decreases markedly. Under the traditional strategy, the wind farm continues to output power close to its rated value, so a substantial imbalance arises between the power injected at the sending end and the power delivered at the receiving end during the fault. This surplus power is consumed mainly by the DC chopper. As a result, the DC voltage rises rapidly at the onset of the fault and repeatedly approaches the 840 kV threshold, causing the chopper to switch frequently. This produces noticeable oscillations in the DC voltage, the sending-end AC voltage, and the DC current. Although the traditional strategy limits the further rise of the DC overvoltage, it is essentially a passive, post-fault dissipation control approach. It does not reduce the power surplus at the source during the fault, so the transient impact on the system remains relatively large.

In contrast, once the proposed strategy detects the rise in the wind turbine outlet voltage, the active power reduction control loop is automatically activated. It quickly reduces the active power output of the wind farm, lowering the active power delivered by the DRU to the DC line to about 540 MW. This value matches the active power that can be delivered to the receiving-end grid during the fault, effectively relieving the power surplus in the DC system. Throughout the fault, the DC voltage is kept below 840 kV, and the DC current is reduced to about 0.64 kA, substantially easing the voltage and current stress during the transient. Because the proposed strategy does not rely on repeatedly triggering the DC chopper through the voltage threshold, the DC voltage does not exhibit the periodic oscillation caused by chopper switching under the traditional strategy, and the transient oscillation of the sending-end AC voltage and the DC current is also markedly reduced.

After the fault is cleared, the receiving-end converter station resumes normal DC voltage control, and the DC voltage U_{dc} gradually falls back and stabilizes at its rated value. According to the monotonic coupling relationship between U_{f} and U_{dc} given in Equation (18), the wind turbine outlet voltage U_{f} decreases accordingly. Once U_{f} falls below the threshold U_{f}^{*}, the active power correction ΔP converges continuously to zero under the limiter logic, and the active power reduction control loop is deactivated. Since the active power reference P_{w}^{*} is formed by adding this correction on top of the MPPT command, once ΔP reaches zero, P_{w}^{*} automatically and continuously returns to $P_{\mathrm{w,MPPT}}$, restoring normal MPPT operation. These results show that, compared with the traditional DC-chopper strategy, the proposed strategy provides better overvoltage suppression and improved transient stability.

Table 3 further summarizes the comparison using measurable indicators, including the DC-voltage range during the fault, the DC current during the fault, the transmitted active power during the fault, the voltage/current oscillation behavior, the maximum active-power curtailment relative to the rated capacity, and the recovery time after fault clearance.

Table 3. Comparison of receiving-end AC fault ride-through performance.

Indicator	Proposed Strategy	Traditional Strategy
U_{dc} range during the fault	About 840 kV	Oscillates repeatedly between 800 kV and 840 kV
I_{dc} during the fault	0.64 kA	Close to 1.37 kA (I_{dcN}); periodic oscillation
P_{pcc} during the fault	540 MW	1100 MW
P_{dc} during the fault	540 MW	Close to 1100 MW; periodic oscillation
Maximum active-power curtailment (relative to rated capacity)	51%	0%
Voltage/current oscillation during the fault	None	Periodic oscillation
Recovery of P_{pcc}	No noticeable overshoot; recovery time 90 ms	—

(2) Fault duration 200 ms, voltage drop 80%

At simulation time t = 0.5 s, a symmetrical three-phase voltage drop was applied at the receiving end, lasting 200 ms before being cleared. During the fault, the receiving-end AC voltage dropped by 80%. The voltage threshold U_{f}^{*} was set to 1.05 p.u., corresponding to a margin coefficient k_{n} = 0.167. The response waveforms of the system under the two strategies during the fault are compared in Figure 14.

Under the more severe receiving-end fault, the traditional DC-chopper strategy experiences a larger power imbalance: the wind farm continues to inject active power close to its rated value. So, the DC voltage repeatedly approaches and oscillates around the 840 kV chopper threshold over an extended period, with correspondingly larger swings in the DC current and in the sending-end and receiving-end active power than under the 50%-sag case in Section 5.2.1(1).

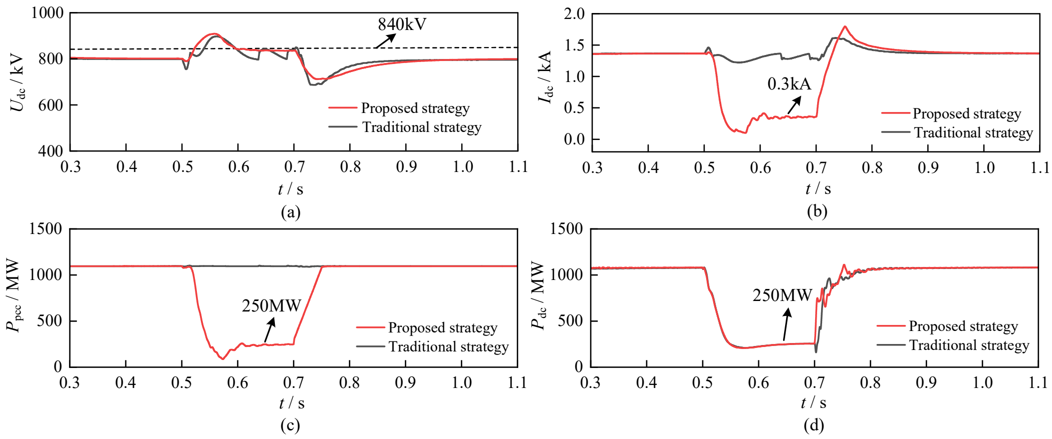

Figure 14. Simulation results of receiving-end AC fault: fault duration 200 ms, voltage drop 80%: (**a**) DC voltage U_{dc}; (**b**) DC current I_{dc}; (**c**) sending-end active power P_{pcc}; (**d**) receiving-end active power P_{dc}.

Under the proposed strategy, the rise in the wind turbine outlet voltage again activates the active power reduction control loop, which curtails the wind farm's active power output considerably further than under the 50%-sag case, down to about 250 MW, in order to match the more severely reduced power that the receiving-end grid can accept during this deeper fault. As a result, the DC current is reduced to about 0.3 kA; although a brief transient occurs near the onset of the fault as the control loop responds, the DC voltage does not settle into the sustained periodic oscillation observed under the traditional strategy, and the system reaches a stable operating condition well before the fault is cleared. These results indicate that, across different fault severities, the proposed strategy consistently allows the wind farm to actively curtail its own power output to match the receiving-end grid's reduced delivery capability, alleviating the DC-side overvoltage at its source rather than relying on passive dissipation.

5.2.2. Receiving-End Single-Line-to-Ground Fault

At simulation time t = 0.5 s, a single-line-to-ground fault was applied at the receiving end, lasting 200 ms before being cleared. The response waveforms of the system under the two strategies are compared in Figure 15.

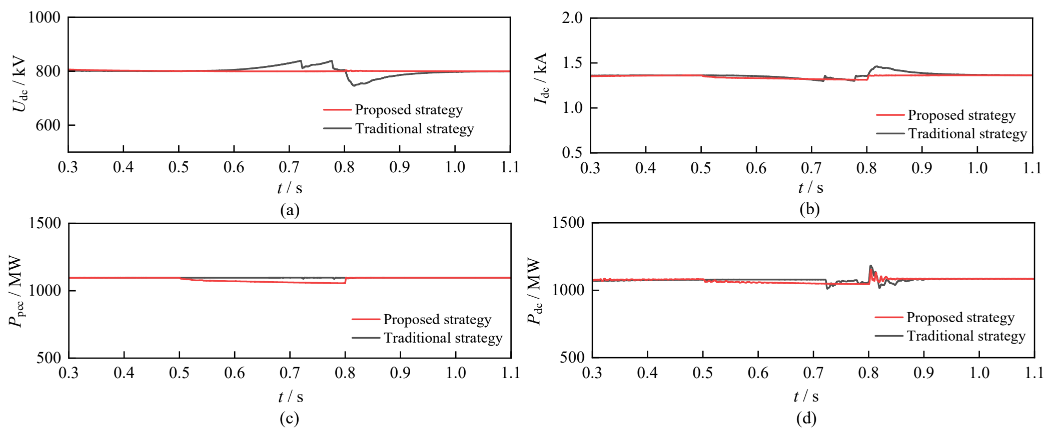

Figure 15. Simulation results of a receiving-end single-line-to-ground fault: (**a**) DC voltage U_{dc}; (**b**) DC current I_{dc}; (**c**) sending-end active power P_{pcc}; (**d**) receiving-end active power P_{dc}.

When a single-line-to-ground fault occurs at the receiving end, the negative-sequence current suppression control already present in the receiving-end converter station effectively isolates the double-frequency ripple caused by the unbalanced fault, so that it does not noticeably affect the DC voltage or DC current. Under the traditional strategy, the fault still creates a power surplus in the DC system, causing U_{dc} to rise. The DC chopper switches frequently to dissipate this surplus power, continuing to produce periodic oscillations in the DC voltage and DC current, similar to the behavior observed under symmetrical receiving-end faults. Under the proposed strategy, each wind farm actively reduces its active power output (Figure 15c), thereby reducing the active power injected into the DC transmission system to match the power that can be delivered to the receiving-end grid, effectively relieving the power surplus in the DC system. Throughout the fault, U_{dc} and I_{dc} remain stable, with no noticeable disturbance.

5.2.3. Influence of System Parameter Variations on Receiving-End Fault Ride-Through Strategy

According to Equation (24), the wind-turbine terminal-voltage limit $U_{f,lim}$ depends on the DC-line resistance R_{dc}, transformer leakage reactance X_d, and current wind-farm operating power ΣP_{wj}. Equation (25) further shows that the terminal-voltage reference U_f^* varies in the same direction as $U_{f,lim}$. The receiving-end voltage-sag depth is not a direct input to these two equations, because the proposed strategy uses closed-loop measurements and detects the resulting power surplus through the measured U_f. The grid-fault condition instead affects the transient trajectories and duration of the control response.

The parameter analysis is performed in two steps. First, ΣP_{wj} is reduced from 1100 MW to 800 MW while R_{dc} = 2 Ω and X_d = 12 Ω remain unchanged. Equations (24) and (25) give $U_{f,lim} \approx 0.895$ kV (1.297 p.u.) and $U_f^* \approx 0.724$ kV (1.05 p.u.), respectively. Thus, within the range considered, changing ΣP_w alone causes only a modest change in the calculated limits. Second, with ΣP_{wj} = 800 MW, R_{dc} and X_d are further increased from 1 Ω and 12 Ω to 9 Ω and 54 Ω, respectively. The recalculated values are $U_{f,lim} \approx 0.927$ kV (1.343 p.u.) and U_f^* ≈ 0.73 kV (1.057 p.u.), indicating a more pronounced influence of the equivalent line and transformer impedances.

An additional simulation is conducted based on the receiving-end fault case in Section 5.2.1(1). The receiving-end voltage-sag depth and fault duration are retained at 50% and 300 ms, respectively. The modified parameters are ΣP_{wj} = 800 MW, R_{dc} = 9 Ω, and X_d = 54 Ω. The simulation results are shown in Figure 16.

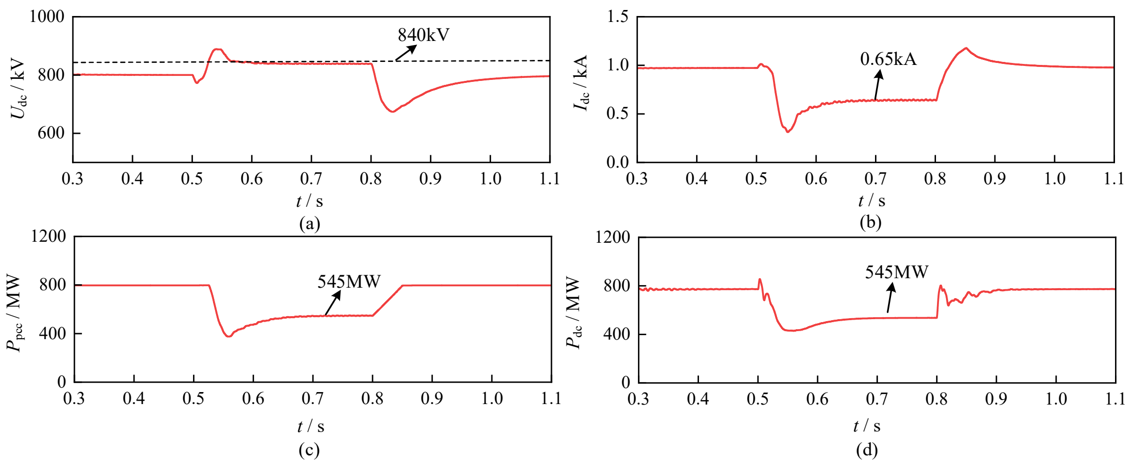

Figure 16. Simulation results under variations in ΣP_{wj}, R_{dc}, and X_d during a receiving-end AC fault: (**a**) DC voltage U_{dc}; (**b**) DC current I_{dc}; (**c**) sending-end active power P_{pcc}; (**d**) receiving-end active power P_{dc}.

As shown in Figure 16, after a brief transient at the fault onset, the DC voltage stabilizes at approximately 840 kV and the DC current settles at approximately 0.65 kA. Accordingly, the sending-end and receiving-end active powers both stabilize at approximately 545 MW, indicating that the source-side power input is effectively matched to the power that can be delivered by the receiving-end converter station during the fault. Therefore, with U_{f}^{*} recalculated as approximately 0.73 kV, the proposed strategy remains effective under the simultaneous variations in wind-farm operating power, DC-line resistance, and transformer leakage reactance.

6. Conclusions

This paper addresses the fault ride-through problem of an offshore wind power transmission system via diode rectifier units under sending-end and receiving-end AC faults. The transient mechanisms of DRU blocking under sending-end faults and DC overvoltage under receiving-end faults were analyzed, and corresponding fault ride-through strategies were proposed. The main conclusions are as follows:

(1) For sending-end AC faults, the relationship between the DC current and the transmitted DC power was established. The proposed active voltage reduction strategy at the receiving-end converter station adaptively lowers the DC voltage reference according to the degree of the DC current drop. It allows the DRU to regain its conduction condition, maintain active power transmission during the fault, and prevent wind turbines from tripping and disconnecting from the grid. Table 4 further compares the proposed strategy with representative existing methods for sending-end faults in terms of control architecture, required measurements, communication needs, hardware requirements, and fault ride-through performance.

Table 4. Comparison of sending-end AC fault ride-through methods.

Method	Control Architecture	Required Measurements	Communication Requirements	Hardware Requirements	Fault Performance
Reference [14]	Crowbar resistor absorbs surplus power	Wind turbine DC bus voltage	Not required	Extra resistor required	Capacitor voltage stable, DRU may still block
Reference [15]	Adaptive current limiting with overcurrent protection	Outlet voltage and current	Not required	Not required	Overcurrent limited, DRU may still block
Reference [16]	Grid-forming control with virtual impedance	Outlet voltage and current	Not required	Not required	Recovery improved, DRU may still block
Proposed	DC current-based active voltage reduction at receiving end	Receiving-end DC current; sending-end voltage U_{pcc}	Required	Not required	DRU stays conducting; power uninterrupted

(2) For receiving-end AC faults, the relationship between the DC voltage and the wind turbine outlet voltage was established. The proposed source-side active power reduction strategy uses the change in the wind turbine outlet voltage to represent the power imbalance and actively reduces the wind farm's power output. It matches the power injected at the sending end to the power that can be delivered at the receiving end during the fault, suppressing the DC overvoltage from the source side. Table 5 further compares the proposed strategy with representative existing methods for receiving-end faults.

(3) Simulation results show that the proposed active voltage reduction strategy avoids DRU blocking and interruption of the power path during sending-end faults, while the active power reduction strategy effectively limits the DC voltage and reduces transient oscillation during receiving-end faults. Both strategies achieve power coordination and voltage stability under different types of AC faults, and both feature a simple control structure with good engineering applicability.

Table 5. Comparison of receiving-end AC fault ride-through methods.

Method	Control Architecture	Required Measurements	Communication Requirements	Hardware Requirements	Fault Performance
Reference [9]	Dissipation resistor absorbs surplus power	DC voltage	Not required	Dissipation device required	Overvoltage limited, repeated oscillation
Reference [11]	Active DC voltage boosting	DC voltage	Not required	Not required	Overvoltage eased, power not reduced
Reference [17]	Voltage boosting plus reduced turbine port voltage	DC voltage, turbine outlet voltage	Required	Not required	Transmission weakened, power not reduced at source
Proposed	Turbine voltage-based active power reduction	Turbine outlet voltage, aggregate active power of wind farms	Required	Not required	Overvoltage suppressed at source, no oscillation

Author Contributions: Conceptualization, J.L.; methodology, J.L.; software, W.L. (Wenxuan Lyu); validation, S.X. and W.L. (Wenxuan Lyu); formal analysis, J.L.; investigation, S.X.; resources, W.L. (Wei Li); writing—original draft preparation, J.L.; writing—review and editing, S.X., W.L. (Wenxuan Lyu) and W.L. (Wei Li); visualization, W.L. (Wenxuan Lyu); supervision, W.L. (Wei Li); project administration, W.L. (Wei Li); funding acquisition, S.X. All authors have read and agreed to the published version of the manuscript.

Funding: This research was funded by the Science and Technology Project of State Grid Jiangsu Electric Power Co., Ltd., grant number J2025001.

Data Availability Statement: The original contributions presented in the study are included in the article. Further inquiries can be directed to the corresponding author.

Acknowledgments: The authors would like to thank the State Grid Jiangsu Electric Power Co., Ltd. Research Institute for its support of this work.

Conflicts of Interest: All authors were employed by the company State Grid Jiangsu Electric Power Co., Ltd. They declare that the research was conducted in the absence of any commercial or financial relationships that could be construed as a potential conflict of interest. The authors declare that this study received funding from State Grid Jiangsu Electric Power Co., Ltd. The funder was not involved in the study design, collection, analysis, interpretation of data, the writing of this article or the decision to submit it for publication

Appendix A

The PI gains of the two proposed outer loops are selected following standard practice for cascaded power-converter control. Their response speed is coordinated with the response speed of the existing inner and outer loops of the wind turbine converter and the receiving-end converter station.

Specifically, the gains k_{ip} and k_{ii} of the active voltage reduction control loop are selected so that the response time of U_{dc}^{*} matches the time scale of the receiving-end converter station's existing outer loop. The adjustment speed of U_{dc}^{*} should match the time-scale range. The range is roughly 10–20 times the current inner-loop time scale, which is a few milliseconds. The resulting time scale for U_{dc}^{*} is therefore on the order of tens of milliseconds [24].

Similarly, the gains k_{up} and k_{ui} of the active power reduction control loop are selected so that the response time of P_{w}^{*} matches the time scale of the wind turbine's existing power outer loop. The response speed of P_{w}^{*} should match the outer-loop time scale, which is roughly 10 times the wind turbine's current inner-loop time scale of about 10 ms. The resulting time scale for P_{w}^{*} is therefore on the order of hundreds of milliseconds [25].

Table A1 lists the PI parameters used in the simulation of this paper. In addition to the two newly proposed outer loops, the table includes the current inner loop, the voltage inner loop, and the power outer loop of the wind turbine grid-side converter. It also includes the DC current inner loop and the DC voltage outer loop of the receiving-end converter station.

Table A1. PI control parameters used in this simulation.

Converter	Control Loop	K_p	K_i
Wind turbine grid-side converter	Current inner loop	5.5	200
	Voltage inner loop	0.6	10
	Active power outer loop	7	20
	Active power reduction control loop	20	500
Receiving-end converter station	DC current inner loop	0.5	333.33
	DC voltage outer loop	20	200
	Active voltage reduction control loop	16	50

References

1. Tang, C.; Li, Y.; Li, H.; Liu, R.; Liu, Z.; Pan, X.; Yang, Q.; Xiao, H. Coordinated Inertia Support Strategy for Offshore Wind Power-Integrated MMC-HVDC System. *Electronics* **2026**, *15*, 1063. [CrossRef]
2. Deng, J.; Cheng, F.; Yao, L.; Xu, J.; Mao, B.; Li, X.; Chen, R. A review of system topologies, key operation and control technologies for offshore wind power transmission based on HVDC. *IET Gener. Transm. Distrib.* **2023**, *17*, 3345–3363. [CrossRef]
3. Jin, Y.; Zhang, Z.; Huang, Y.; Xu, Z.; Xu, F. Harmonic filtering and fault ride-through of diode rectifier unit and modular multilevel converter based offshore wind power integration. *IET Renew. Power Gener.* **2023**, *17*, 3554–3567. [CrossRef]
4. Yang, Z.; Wang, X.; Zou, K.; Jiang, C. Mid-frequency oscillation suppression methodology for offshore wind power VSC-HVDC system and its engineering validation. *Electr. Power Eng. Technol.* **2025**, *44*, 109–116.
5. Guo, G.; Wang, H.; Song, Q.; Zhang, J.; Wang, T.; Ren, B.; Wang, Z. HB and FB MMC Based Onshore Converter in Series-Connected Offshore Wind Farm. *IEEE Trans. Power Electron.* **2020**, *35*, 2646–2658. [CrossRef]
6. Chen, H.; Li, Z.; Du, W.; Wang, H. Reduced-order method and oscillation risk assessment for renewable energy with VSC-HVDC system. *Electr. Power Eng. Technol.* **2026**, *45*, 26–38.
7. Lu, Y.; You, J.; Li, Z.; Qiu, F.; Ye, W.; Zhang, Z.; Xu, Z. Heterogeneous DC Transmission System for Offshore Wind Power Based on the Parallel Operation of MMC-HVDC and DRU-HVDC. *Electronics* **2026**, *15*, 2991. [CrossRef]
8. Bernal-Perez, S.; Ano-Villalba, S.; Blasco-Gimenez, R.; Rodriguez-D'Derlee, J. Efficiency and Fault Ride-Through Performance of a Diode-Rectifier- and VSC-Inverter-Based HVDC Link for Offshore Wind Farms. *IEEE Trans. Ind. Electron.* **2013**, *60*, 2401–2409. [CrossRef]
9. Liang, P.; Pei, X.; Zhou, Y.; Wu, H.; Xu, Y.; Zhang, Z.; Xu, Z.; Qiu, F. Harmonic Analysis and Elimination of Transmission Scheme Based on DRU for Medium-Frequency Offshore Wind Farms. *Electronics* **2025**, *14*, 3669. [CrossRef]
10. Bidadfar, A.; Saborio-Romano, O.; Cutululis, N.A.; Sorensen, P.E. Control of Offshore Wind Turbines Connected to Diode Rectifier-Based HVdc Systems. *IEEE Trans. Sustain. Energy* **2021**, *12*, 514–523. [CrossRef]
11. Yu, L.; Li, R.; Xu, L. Distributed PLL-based control of offshore wind turbines connected with diode-rectifier-based HVDC systems. *IEEE Trans. Power Deliv.* **2018**, *33*, 1328–1336. [CrossRef]
12. Zhang, Z.; Jin, Y.; Xu, Z. Two offshore wind farm integration schemes based on grid forming wind turbines and diode rectifier unit. *High Volt. Eng.* **2022**, *48*, 2098–2107.
13. Xiao, H.; Huang, X.; Huang, Y.; Liu, Y. Self-Synchronizing Control and Frequency Response of Offshore Wind Farms Connected to Diode Rectifier Based HVDC System. *IEEE Trans. Sustain. Energy* **2022**, *13*, 1681–1692. [CrossRef]
14. Yu, H.; Cai, X.; Yang, R.; Yang, M.; Tang, G. Analysis of Electrical Regulation Characteristics and Group Grid-Forming Control Strategy of DRU-HVDC Integrated Offshore Wind Farm. *Proc. CSEE* **2025**, *45*, 2318–2334.
15. Li, R.; Yu, L.; Xu, L. Offshore AC fault protection of diode rectifier unit-based HVdc system for wind energy transmission. *IEEE Trans. Ind. Electron.* **2019**, *66*, 5289–5299. [CrossRef]
16. Zhang, Y.; Zhu, W.; Tang, C.; Liu, N.; Li, S.; Wang, H. Start-Up and Fault-Ride-Through Strategy for Offshore Wind Power via DRU-HVDC Transmission System. *Energies* **2024**, *17*, 4968. [CrossRef]
17. Yang, M.; Cai, X.; Wusiman, A.; Zhang, J.; Lyu, J. Distributed-Diode-Rectifiers-Based Offshore Wind Power MVDC Direct-Transmission System. *IEEE Trans. Energy Convers.* **2022**, *37*, 643–653. [CrossRef]
18. Xiao, H.; Huang, X.; Li, Y.; Huang, W.; Cai, D.; Peng, F. Reactive Power-Synchronization Control for Offshore Wind Turbines Connected to Diode Rectifier. *High Volt. Eng.* **2022**, *48*, 3820–3828.

19. Zhang, Z.; Xu, Z. Design and DC fault clearance of modified hybrid MMC with low proportion of full-bridge submodules. *IET Gener. Transm. Distrib.* **2021**, *15*, 2203–2214. [CrossRef]
20. Guo, M.; Hao, Q.; Ding, L. Improved AAVM and Small-Signal Model of Hybrid MMC Considering Dynamic Differences Between Full-Bridge and Half-Bridge Submodules. *IEEE Trans. Power Electron.* **2024**, *39*, 8215–8228. [CrossRef]
21. Du, C.; Zhang, Q.; Cao, S. A Smart Fault-Tackling Strategy Based on PFTE for AC Three-Phase-to-Ground Faults in the Multi-Terminal HVDC Wind Power Integration System: Further Foundings. *Energies* **2022**, *15*, 768. [CrossRef]
22. Yu, L.; Fu, Z.; Zhu, J.; Li, R.; Peng, G.; Zhao, C. Review on Grid-forming Control and Start-up Method of Diode-rectifier-unit Based HVDC Transmission System for Remote Offshore Wind Farm. *Autom. Electr. Power Syst.* **2023**, *47*, 63–79.
23. Brochu, J.; Larose, C.; Gagnon, R. Generic Equivalent Collector System Parameters for Large Wind Power Plants. *IEEE Trans. Energy Convers.* **2011**, *26*, 542–549. [CrossRef]
24. Lu, X.; Chen, W.; Li, K.; Zhang, G.; Yu, H. Evaluation of Power Carrying Capacity Limits and Parameter Stability Regions at the PCC of MMC-HVDC System. *Power Syst. Technol.* **2026**, *50*, 2783–2793.
25. Huang, M.; Shu, S.; Li, X.; Fu, X.; Zha, X. A Review of Synchronization-Stability-Oriented Analysis and Control of Power Electronic Grid-Connected Converters. *Trans. China Electrotech. Soc.* **2024**, *39*, 5978–5994.

https://doi.org/10.3390/electronics15184201